Speed/Torque Ripple Reduction of High-speed Permanent Magnet Starters/Generators with Low Inductance for More Electric Aircraft Applications

Xiang Zhang, Tao Yang, *Senior Member, IEEE* and Serhiy Bozhko, *Senior Member, IEEE*

***Abstract*— With the electrification trend of future aircraft, high-speed Permanent Magnet Starters/Generators (PMS/Gs) will potentially be widely used in onboard generation systems due to their high power density and high efficiency. However, the per-unit reactance of such high-speed machines is normally designed to be very low due to limited onboard power supply voltage and large electrical power demand, which can result in large current ripples in the machine and thus large torque ripples especially when the machine is fed with a semiconductor-based inverter of a lower switching frequency. The torque ripples may further lead to speed oscillation and generate severe vibrations and noises that are harmful to the mechanical system and human beings around. In this paper, a speed/torque ripple reduction method for high-speed PMS/Gs with a low inductance is proposed to improve their performance within a wide speed range. An active damping technique is applied to the speed loop to increase the anti-disturbance capability and generate a smoother reference for the current loop, whereas an adaptive output voltage saturation limit is utilized for the current loop to limit the peak value of current to prevent over-current and torque spikes. The parameter tuning criteria is derived through a thorough analysis. Finally, the proposed method is validated on a high-speed PMS/G with an inductance of 99uH. The results show that the speed ripples and torque ripples are reduced by over 50% within a speed range of 2 krpm to 14 krpm.**

***Index Terms*— speed/torque ripple reduction, high-speed starter/generator, low inductance, active damping, adaptive saturation limit**

I. Introduction

Reduction of greenhouse gas emissions is more mandatory now than before. The aviation sector contributes significantly to these emissions, where the sector's CO2 emissions resembled 2.2% of the global CO2 emissions in 2017 [1]. The conventional aircraft system is complex, and the multiple power-conversion steps reduce the entire system's efficiency and reliability [2]. Electrical systems are more and more widely implemented in more electric aircraft (MEA) over the last few decades due to their potential in improving efficiency and reducing emissions [3-4]. Many subsystems that previously used to be driven by hydraulic, mechanical, and pneumatic power have been fully or partially replaced with electrical systems [1]. As the aerospace industry keeps moving toward greener and more electric solutions [5, 6], electrical systems on aircraft will continue to play an ever-increasing role [7].

A key technology of the MEA is the electrical drive system that serves as the interface between the aircraft engine and the onboard electrical power system [8]. An electrical drive system can operate as a starter/generator (S/G) for the MEA with the appropriate power converter, electrical machine, and control scheme. An electrical machine can be used as a starter to drive the aircraft engine and can alternatively function as a generator when the engine drives the electrical machine [9]. The S/G system may simplify the power generation system by reducing the complexity of the mechanical subsystem, especially in aerospace and automotive applications, which would result in increased reliability and reduced overall weight [10]. Among its counterparts, high-speed permanent magnet starter/generators (PMS/Gs) have been a popular candidate due to their high power density and flexible bidirectional operation, which contributes to high instant power/torque output and better efficiency over a wide speed range [11–14].

However, the PMS/Gs are expected to deliver hundreds of kW electrical power as a generator due to the increasing electric demand of MEA and operate at a wide speed range as a starter to drive the engine to the ignition speed [15]. To achieve high power density in a 270V onboard DC power supply system, electrical machines for aerospace applications are preferable of higher speeds (>10,000rpm), larger current density compared to conventional machines and multiple pole pairs. The high fundamental frequency would result in the increase of coil resistance and decrease of coil inductance due to proximity and skin effect [16]. Moreover, the increased effective airgap in surface mounted PMS/Gs and low coil turn count due to multiple pole design attempts result in a low inductance of the high-speed PMS/Gs. As a result, the high-speed PMS/Gs are normally with low inductance and resistance. The downside

This work was supported by the Clean Sky 2 Joint Undertaking under the European Union's Horizon 2020 research and innovation programme under grant agreement number 820913 and 831914. *(Corresponding authors: Tao Yang).*

Xiang Zhang is with the Power Electronics, Machines and Controls Research Group, University of Nottingham, Nottingham NG7 2RD, U.K. and Turntide Technologies, Gateshead NE11 0QA, U.K. (e-mail: Xiang.Zhang@nottingham.ac.uk, Sean.Zhang@turntide.com).

Tao Yang is with the Power Electronics, Machines and Controls Research Group, University of Nottingham, Nottingham NG7 2RD, U.K. (e-mail: Tao.Yang@nottingham.ac.uk).

Serhiy Bozhko is with the with the Power Electronics, Machines and Controls Research Group, University of Nottingham, Nottingham NG7 2RD, U.K. (e-mail: Serhiy. Bozhko@Nottingham.ac.uk).

part of low inductance in the machine is that when these machines are fed with semiconductor-based AC/DC converters, torque ripples resulting from distorted AC currents become significant, especially when the modulation ratio (modulation frequency over fundamental frequency of the machine) is low [17]. In severe cases, the torque ripples may lead to speed oscillation and generate severe vibrations and noises that are harmful to the mechanical system and human beings around. In addition, the low inductance and resistance also increase the risk of overcurrent in case of current controller saturation, especially at low speed when the back electromotive force (back-EMF) is relatively lower.

Although the application of widegap devices with higher switching frequency to an inverter can significantly reduce torque ripples and speed ripples, it is still worthwhile if a modified control method can effectively improve the performance of an inverter based on IGBTs to a satisfactory level. The price of widegap devices is 5 to 10 times or even more than that of conventional devices with the same voltage and current. The requirements for the drive circuit and the accessory circuit also become higher. The multilevel converter can be adopted with a reduced voltage drop of each power device, but the number of power devices increases significantly resulting in increased system volume and cost and more complex control algorithms [18]. Apart from the higher device and drive circuit cost, higher switching loss and more significant EMI issues of the widegap devices, the increase of switching frequency would result in the reduction of allowed computation time for the microcontroller between sampling of current feedbacks and updating of voltage references from the control perspective. As a result, more advanced microcontrollers with higher computation speed need to be used, which in turn increases the cost of the overall system.

Many torque ripple reduction methods for high-speed PMSMs have been published in the literature in recent years. In [19], the cogging torque of a high-speed PMSM is mitigated through a closed slot design to reduce the 11th and 13th harmonics of air-gap flux and weaken the slotting effect. In [20], the reluctance torque ripple and cogging torque are reduced through the magnet shifting technique. In [21] and [22], torque ripples are identified or measured offline to be compensated through a tailored lookup table. Similarly, periodic torque ripples are observed by a repetitive observer [23-25] or isolated by iterative learning control [26, 27] in real time and compensated accordingly. In [28] and [29], torque ripples caused by distorted back electromotive and non-sinusoidal flux distribution are settled by tailoring the current reference according to offline measured the back-EMF and inductances of the motor. Torque ripples due to current harmonics and parameter mismatches in direct torque control (DTC) [30-32] and model predictive control (MPC) [33, 34] are reduced through optimized modulation methods and improved torque or current control accuracy. All these methods aim to solve some torque ripples from a specific source through either a change of the motor structure, pre-measurement or online observation of torque ripples or more accurate current control. However, few papers are particularly focused on speed and torque ripples resulting from the low inductance of high-speed PMSMs and relatively lower switching frequency of the inverter within the Proportional Integral (PI) based Field Oriented Control (FOC) frame which is most widely used in the industry due to its simple structure and parameter independence.

The contribution of this paper is to fill this gap and develop a modified control technique that can reduce torque ripples and speed ripples of high-speed PMS/Gs with low inductance and relatively lower switching frequency within the PI-based FOC frame to improve their performance within a wide speed range. As the torque ripple is a disturbance of the speed loop, an active damping scheme is applied to the speed loop to increase its anti-disturbance capability and generate a smoother reference for the current loop. Different forms of active damping are compared, based on which parameter tuning criteria are concluded. Overcurrent issues at d,q-axis current controller saturation are considered, from which an adaptive reference voltage saturation limit is proposed and a back-calculation anti-windup strategy is utilized for the current loop to limit the peak value of current to prevent torque spikes and speed oscillations. The proposed adaptive saturation limit in combination with the active damping scheme can reduce the torque and speed ripples by over 50% and thus effectively reduce the noises and vibrations.

The paper is organized as follows. The deciding factors of torque ripples are analyzed in Section II. The proposed torque ripple reduction method is elaborated in Section III, whereas simulation results on a tradeoff study in comparison with widegap devices are presented in Section IV. In Section V, the performance of the proposed strategy is validated on a high-speed PMS/G with the inductance of 99uH within a speed range from 2 krpm to 14 krpm. At last, a conclusion is drawn in Section VI.

II. Torque ripple analysis

The mathematical model of PMS/Gs in the synchronous rotating frame is listed as Equations (1)-(4),

$$\frac{di_d}{dt} = \frac{1}{L_d}(v_d - R_s i_d + \omega_r L_d i_d) \tag{1}$$

$$\frac{di_q}{dt} = \frac{1}{L_q}(v_q - R_s i_q - \omega_r L_d i_d - \omega_r \psi_m) \tag{2}$$

$$T_\mathrm{e} = \frac{3}{2}P\left[\left(L_d - L_q\right)i_d i_q + \psi_\mathrm{m} i_q\right] \tag{3}$$

$$J\frac{d\omega_m}{dt} = T_\mathrm{e} - K_f\omega_m - T_L \tag{4}$$

where i_d and i_q denote the d and q axis currents, whereas v_d and v_q are the d and q axis voltages, respectively. L_d and L_q are the d and q axis inductance, respectively. ψ_m is the flux linkage. ω_r and ω_m are the electrical and mechanical angular velocities, respectively. T_e and T_L are the electrical magnetic torque and mechanical torque, respectively. J and K_f are the inertia and frictional damping ratio. Considering a surface-mounted PMS/G, $L_d = L_q$, the derivative of (3) can be given as

$$\frac{dT_\mathrm{e}}{dt} = \frac{3}{2}P\psi_\mathrm{m}\frac{di_q}{dt} + \frac{3}{2}Pi_q\frac{d\psi_\mathrm{m}}{dt} \tag{5}$$

Substituting (2) into (5) and assuming the flux linkage is constant, (6) is derived as

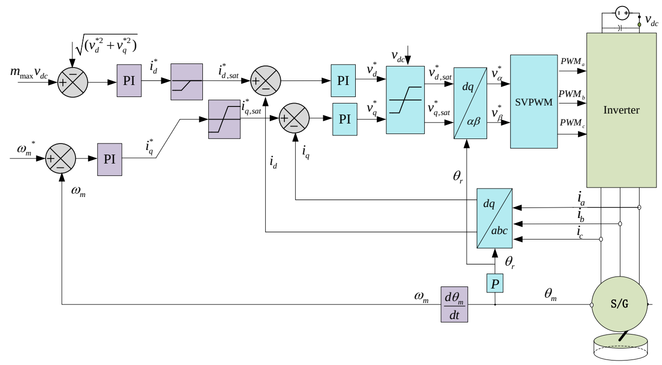

Fig.1 Diagram of a conventional PI-based FOC method

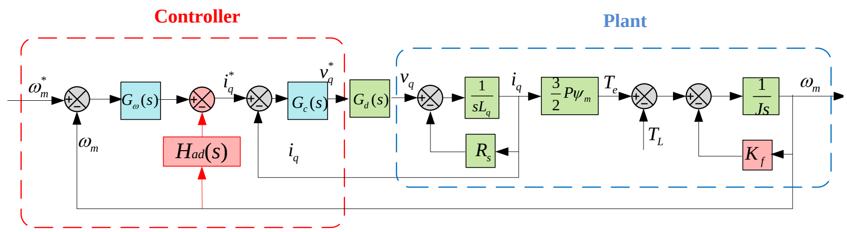

Fig.2 Control loop with active damping *$H_{ad}(s)$*

$$\frac{dT_{\mathrm{e}}}{dt}=\frac{3P\psi_{\mathrm{m}}}{2L_{\mathrm{q}}}(v_q - R_s i_q - \omega_r L_d i_d - \omega_r \psi_{\mathrm{m}}) \qquad (6)$$

Considering the machine is fed by a DC/AC inverter, with the switching behavior of the inverter, using (6), the torque ripple in a certain switching period can be expressed as

$$\Delta T_e(k)=\frac{3}{2}P\frac{\psi_{\mathrm{m}}}{f_s L_{\mathrm{q}}}(v_q(k) - R_s i_q(k) - \omega_r(k) L_d i_d(k) - \omega_r(k)\psi_{\mathrm{m}}) \qquad (7)$$

where the number k denotes the average value of the state variable in the k^th switching period, whereas f_s denotes the switching frequency. It can be concluded that the torque ripple is proportional to $P\psi_{\mathrm{m}}/(f_s L_{\mathrm{q}})$. For comparison studies, parameters of two high-speed PMS/Gs are listed in Table I and Table II, respectively. PMS/G-I is driven by a SiC MOSFET based inverter with a switching frequency of 40 kHz and phase inductance of 874 uH, whereas PMS/G-II [33] is driven by a Silicon IGBT based inverter with a switching frequency of 16 kHz and phase inductance of 99 uH. The $P\psi_{\mathrm{m}}/(f_s L_{\mathrm{q}})$ value of PMS/G-II is 12.2 times of PMS/G-I, which means the torque ripple of PMS/G-II can be 12.2 times of PMS/G-I if the same voltage is applied to the q-axis inductance. For a high-speed PMS/G with low inductance and limited switching frequency like PMS/G-II, a possible way is to reduce the torque ripple through control strategies is to limit the q-axis voltage and d, q-axis currents at each switching interval.

TABLE I
PARAMETERS OF THE PMSM/G-I

Pole Pairs	6
Stator Resistance (Ω)	0.46
Stator Inductance (uH)(Ld=Lq)	874
Flux Linkage (V.s)	0.033
Rated Speed (rpm)	12400
Rated Power(kW)	20.0
Rated Current Amplitude(A)	38.5
Rated torque(N*m)	17.0
DC-link Voltage (V)	540
Switching Frequency (kHz)	40
Sampling Frequency(kHz)	40

TABLE II
PARAMETERS OF THE PMSM/G-II

Pole Pairs	3
Stator Resistance (Ω)	0.1
Stator Inductance (uH)(Ld=Lq)	99
Flux Linkage (V.s)	0.0364
Rated Speed (rpm)	18000
Rated Current Amplitude(A)	145.8
Rated Power(kW)	45.0
Rated Torque(N*m)	23.5
DC-link Voltage (V)	270
Switching Frequency (kHz)	16
Sampling Frequency(kHz)	16

Fig.1 shows the control diagram of a PMS/G at the starter mode, which is the commonly used field-oriented cascaded PI control with flux weakening control. The internal control loop is for the d,q-axis current control and the outer loops are for speed and flux weakening control. For generator operation of the PMS/G, the speed loop will be replaced by the dc-link voltage control or droop control [35].

The speed and current loop controllers in Fig.1 are expressed as

$$i_q^* = k_{p\omega}(1+\frac{1}{T_{\omega}s})(\omega_m^* - \omega_m) \qquad (8)$$

$$v_d^* = k_{pi}\left(1+\frac{1}{T_i s}\right)(i_d^* - i_d) - \omega_r L_q i_q \qquad (9)$$

$$v_q^* = k_{pi}\left(1+\frac{1}{T_i s}\right)\left(i_q^* - i_q\right) + \omega_r(\psi_m + L_d i_d) \qquad (10)$$

As the q-axis current reference is generated by the speed loop controller, any speed fluctuation would result in current reference ripples (from (8)) and voltage reference ripples (10). This in turn leads to torque ripples and further increases the speed ripples.

Therefore, a properly designed speed controller, reducing the ripples in i_q^*, can potentially reduce the torque ripples. Also, the q-axis voltage needs to be dynamically adjusted with the variation of speed and cross-coupling voltages to prevent over-current, which is normally realized by the integral action of the PI controller. However, a larger integral gain may easily lead to the current controller saturation since the d, q-axis current cannot track the reference in a transient response due to the cross-coupling voltage especially when the error between current reference and feedback is large, which happens at sudden load changes. At saturation conditions, the voltage reference is clamped to the maximum modulated voltage of the inverter, which is $1/\sqrt{3}$ of DC-link voltage for Space Vector Pulse Width Modulation (SVPWM) or 1/2 of DC-link voltage for Sinusoidal Pulse Width Modulation (SPWM). The saturation can cause severe over-current of PMSM/Gs at a lower speed with lower back-EMF due to low inductance and resistance, and thus results in instant torque spikes and speed overshoot. To settle these issues, a control algorithm with active damping and adaptive saturation limit is proposed in Section III.

III. THE PROPOSED MODIFICATIONS AND PERFORMANCE ANALYSIS

A. Active Damping for the speed loop

The concept of virtual resistor or active damping was proposed by P. A. Dahono in 2002, for the application of input LC filter of PWM converter [36] and then for LCL filter of DC/DC converter [37] to dampen the LC resonance. A resistor can be connected in various ways to dampen the oscillation in the LC/LCL circuit, but the power loss is thereby increased. The idea of active damping or virtual resistor can be generalized as the effect of a real resistor can be replaced by an equivalent control strategy. In this way, the damping effect can be realized, but the power loss with a real resistor can be avoided.

In this paper, this idea of active damping is transplanted to the speed loop of high-speed PMS/Gs. Unlike most literature dealing with the torque ripples by direct harmonic rejection, an indirect way through improving the anti-disturbance capability of speed loop by active damping is used to reduce speed ripples and generate a smoother current reference and thus reduce torque ripples. The control loop diagram of the PMS/G with the active damping scheme is presented in Fig.2, where the left side block is the controller, and the right side represents the PMS/G plant. The damping ratio K_f of the plant is very small for low mechanical loss, which results in a very small integral gain and weak anti-disturbance capability for the PI controller designed based on pole-zero cancellation criteria. However, a lot of disturbance in the speed loop (lumped as T_L in Fig.2) such as torque ripples, load torque and other unmodelled uncertainties would deteriorate the stability and dynamic performance of the speed controller. Similar to the virtual resistance effect in current circuits, the virtual damping ratio of the mechanical plant can be increased by adding an active damping term to the output of the speed controller. In Fig.2, an active damping term $-H_{ad}(s)\omega_m$ is added to the q-axis current reference.

To verify the effectiveness of the active damping scheme, the closed loop tracking and anti-disturbance transfer functions need to be derived and analyzed in the following. With the active damping feedback added to (8), the q-axis current reference i_q^* is given as

$$i_q^* = k_{p\omega}(1+\frac{1}{T_\omega s})(\omega_m^* - \omega_m) - H_{ad}(s)\omega_m \qquad (11)$$

Substituting (11) to (10), the q-axis voltage reference is derived as

$$v_q^* = k_{pi}\left(1+\frac{1}{T_i s}\right)\left(k_{p\omega}\left(1+\frac{1}{T_\omega s}\right)(\omega_m^* - \omega_m) - H_{ad}(s)\omega_m - i_q\right) + \omega_r(\psi_m + L_d i_d) \qquad (12)$$

Assuming the current controller is not saturated, i.e. $v_q = v_q^*$ and solving the equation by substituting (11) into (2) , i_q can be obtained as

$$i_q = \frac{\frac{k_{pi}}{L_q}\left(1+\frac{1}{T_i s}\right)\left(k_{p\omega}\left(1+\frac{1}{T_\omega s}\right)(\omega_m^*-\omega_m) - H_{ad}(s)\omega_m\right)}{s+\frac{R_s}{L_q}+\frac{k_{pi}}{L_q}\left(1+\frac{1}{T_i s}\right)} \qquad (13)$$

Substituting (13) into (3), the mechanic equation of the machine is derived as

$$\left(s+\frac{R_s}{L_q}+\frac{k_{pi}}{L_q}\left(1+\frac{1}{T_i s}\right)\right)\left(s+\frac{K_f}{J}\right)\omega_m = \frac{3P\psi_m}{2}\frac{k_{p\omega}k_{pi}}{JL_q}\left(1+\frac{1}{T_i s}\right)\left(1+\frac{1}{T_\omega s}\right)\omega_m^* - \frac{3P\psi_m}{2}\frac{k_{pi}}{JL_q}\left(1+\frac{1}{T_i s}\right)\left(H_{ad}(s)+k_{p\omega}\left(1+\frac{1}{T_\omega s}\right)\right)\omega_m - \frac{T_L}{J}\left(s+\frac{R_s}{L_q}+\frac{k_{pi}}{L_q}\left(1+\frac{1}{T_i s}\right)\right) \qquad (14)$$

As ω_m is determined by two factors, the reference ω_m^* and the disturbance T_L , the corresponding transfer functions are analyzed separately according to the superposition principle. The closed-loop tracking transfer function ω_m/ω_m^* is derived as

$$\frac{\omega_m}{\omega_m^*} = \frac{\frac{3P\psi_m}{2}\frac{k_{p\omega}k_{pi}}{JL_q}\left(s+\frac{1}{T_i}\right)\left(s+\frac{1}{T_\omega}\right)}{s\left(s^2+\frac{R_s}{L_q}s+\frac{k_{pi}}{L_q}\left(s+\frac{1}{T_i}\right)\right)\left(s+\frac{K_f}{J}\right)+\frac{3P\psi_m}{2}\frac{k_{pi}}{JL_q}\left(s+\frac{1}{T_i}\right)\left(H_{ad}(s)s+k_{p\omega}\left(s+\frac{1}{T_\omega}\right)\right)} \qquad (15)$$

whereas the closed-loop anti-disturbance transfer function ω_m/T_L is derived as

$$\frac{\omega_m}{T_L} = -\frac{\frac{1}{J}s\left(s^2+\frac{R_s}{L_q}s+\frac{k_{pi}}{L_q}\left(s+\frac{1}{T_i}\right)\right)}{\left(s^2+\frac{R_s}{L_q}s+\frac{k_{pi}}{L_q}\left(s+\frac{1}{T_i}\right)\right)\left(s+\frac{K_f}{J}\right)+\frac{3P\psi_m}{2}\frac{k_{pi}}{JL_q}\left(1+\frac{1}{T_i s}\right)\left(H_{ad}(s)s+k_{p\omega}\left(s+\frac{1}{T_\omega}\right)\right)} \qquad (16)$$

The closed-loop tracking transfer function ω_m/ω_m^* is 4th-order with 4 poles and 2 zeros, whereas the closed-loop anti-disturbance transfer function is 4th-order with 4 poles and 3 zeros. Both can be reduced to 2nd-order through pole-zero cancellation by properly choosing the form of $H_{ad}(s)$ and tuning the PI parameters to improve the controller stability. In this paper, two different forms of active damping will be discussed. As proportional feedback is the most used active damping form in LCL applications, it's analyzed first as Case 1. Then a proportional and differential feedback active damping is analyzed as Case 2. These two cases will be compared with the original speed controller without active damping (Case3) as follows.

Case 1: $H_{ad}(s) = \frac{K_{fa} - \widehat{K_f}}{\frac{3}{2}P\psi_{\mathrm{m}}}$

The simplest and most commonly used way to realize active damping is to apply proportional feedback with $H_{ad}(s) = \frac{K_{fa} - \widehat{K_f}}{\frac{3}{2}P\psi_{\mathrm{m}}}$, where K_{fa} is the expected virtual damping ratio of the speed loop after active damping is applied, and $\widehat{K_f}$ is the estimated value of K_f in (4). The PI parameters are set as $k_{p\omega} = \frac{2\pi f_\omega \hat{J}}{\frac{3P\psi_m}{2}}$, $T_\omega = \frac{\hat{J}}{K_{fa}}, k_{pi} = 2\pi f_c \widehat{L_q}$, $T_i = \frac{\widehat{L_q}}{\widehat{R_s}}$, for pole-zero cancellation, where parameters with '$\widehat{\ }$' represents corresponding parameters used in the controller which can potentially be different from the real values in the plant, and f_ω and f_c are the bandwidth of the speed loop and current loop, respectively. Then (15) is transformed to (17)

$$\frac{\omega_m}{\omega_m^*} = \frac{4\pi^2 f_c f_\omega \frac{\widehat{L_q}\hat{J}}{L_q J}\left(s+\frac{\widehat{R_s}}{\widehat{L_q}}\right)\left(s+\frac{K_{fa}}{\hat{J}}\right)}{s\left(s^2+\frac{R_s}{L_q}s+2\pi f_c\frac{\widehat{L_q}}{L_q}\left(s+\frac{\widehat{L_q}}{\widehat{R_s}}\right)\right)\left(s+\frac{K_f}{J}\right)+2\pi f_c\frac{\widehat{L_q}}{L_q}\left(s+\frac{\widehat{L_q}}{\widehat{R_s}}\right)\left(\left(\frac{K_{fa}}{\hat{J}}-\frac{\widehat{K_f}}{\hat{J}}\right)s+2\pi f_\omega\frac{\hat{J}}{J}\left(s+\frac{K_{fa}}{\hat{J}}\right)\right)} \tag{17}$$

$$\frac{\omega_m}{\omega_m^*} = \frac{4\pi^2 f_c f_\omega \frac{\widehat{L_q}\hat{J}}{L_q J}\left(s+\frac{K_{fa}}{\hat{J}}\right)}{s^2\left(s+2\pi f_c\frac{\widehat{L_q}}{L_q}\right)+s\left(\frac{K_f}{J}s+\frac{\widehat{L_q}}{L_q}\left(\frac{K_{fa}}{\hat{J}}-\frac{\widehat{K_f}}{\hat{J}}\right)s+2\pi f_c\frac{\widehat{L_q}}{L_q}\frac{K_{fa}}{\hat{J}}\right)+4\pi^2 f_c f_\omega\frac{\widehat{L_q}\hat{J}}{L_q J}\left(s+\frac{K_{fa}}{\hat{J}}\right)} \tag{20}$$

Assuming parameters used in the controller is close to the real values and thus $\frac{\widehat{L_q}}{\widehat{R_s}} = \frac{\mathrm{L_q}}{R_s}$ and $\frac{\widehat{K_f}}{\hat{J}} = \frac{K_f}{J}$, the pole and zero $s = -\frac{\widehat{\mathrm{R_s}}}{\widehat{\mathrm{L_q}}}$ can be cancelled and (17) is transformed to

$$\frac{\omega_m}{\omega_m^*} = \frac{4\pi^2 f_c f_\omega \frac{\widehat{L_q}\hat{J}}{L_q J}\left(s+\frac{K_{fa}}{\hat{J}}\right)}{s^2\left(s+2\pi f_c\frac{\widehat{L_q}}{L_q}\right)+s\left(\frac{K_f}{J}s+2\pi f_c\frac{\widehat{L_q}}{L_q}\frac{K_{fa}}{\hat{J}}\right)+4\pi^2 f_c f_\omega\frac{\widehat{L_q}\hat{J}}{L_q J}\left(s+\frac{K_{fa}}{\hat{J}}\right)} \tag{18}$$

Similarly, the anti-disturbance transfer function can be derived as

$$\frac{\omega_m}{T_L} = -\frac{\frac{1}{J}s\left(s+2\pi f_c\frac{\widehat{L_q}}{L_q}\right)}{s^2\left(s+2\pi f_c\frac{\widehat{L_q}}{L_q}\right)+s\left(\frac{K_f}{J}s+2\pi f_c\frac{\widehat{L_q}}{L_q}\frac{K_{fa}}{\hat{J}}\right)+4\pi^2 f_c f_\omega\frac{\widehat{L_q}\hat{J}}{L_q J}\left(s+\frac{K_{fa}}{\hat{J}}\right)} \tag{19}$$

The closed-loop tracking transfer and closed-loop, anti-disturbance transfer function are both reduced to 3-rd order with pole-zero $s = -\frac{\widehat{\mathrm{R_s}}}{\widehat{\mathrm{L_q}}}$ cancelled, whereas there is still a zero $s = -\frac{K_{fa}}{\hat{J}}$ in (18) and $s = -2\pi f_c\frac{\widehat{L_q}}{L_q}$ in (19), respectively, without a paired pole to be cancelled. The reason is that active damping is used in the outer loop in this paper, which is different from applying active damping in the inner loop for LCL filters. Therefore, pure proportional feedback is not the best choice, and some modifications can be made to $H_{ad}(s)$ to allow cancellation of one more pole and reduce (18) and (19) to second order.

Case 2: $H_{ad}(s) = \frac{K_{fa} - \widehat{K_f}}{\frac{3}{2}P\psi_{\mathrm{m}}}\left(\frac{s}{2\pi f_c}+1\right)$

If differential feedback is added to the active damping transfer function with $H_{ad}(s) = \frac{K_{fa} - \widehat{K_f}}{\frac{3}{2}P\psi_{\mathrm{m}}}\left(\frac{s}{2\pi f_c}+1\right)$, (18) is replaced by (20). Assuming $\widehat{L_q} = L_q$ which means the accuracy of measured or observed L_q is high enough, (20) can be simplified to a second-order system

$$\frac{\omega_m}{\omega_m^*} = \frac{4\pi^2 f_c f_\omega \frac{\hat{J}}{J}}{\left(s+2\pi f_\omega\frac{\hat{J}}{J}\right)(s+2\pi f_c)} \tag{21}$$

with the paired pole-zero $s = -\frac{K_{fa}}{\hat{J}}$ cancelled.

Similarly, the closed-loop anti-disturbance transfer function ω_m/T_L is also reduced to second order

$$\frac{\omega_m}{T_L} = -\frac{\frac{1}{J}s}{\left(s+2\pi f_\omega\frac{\hat{J}}{J}\right)\left(s+\frac{K_{fa}}{J}\right)} \tag{22}$$

with the paired pole-zero $s = -2\pi f_c\frac{\widehat{L_q}}{L_q}$ cancelled.

Case 3: $H_{ad}(s) = 0$

For comparison studies, the conventional PI-based strategy without active damping can be regarded as a special case $H_{ad}(s) = 0$, then the closed-loop tracking and anti-disturbance transfer functions can be obtained as

$$\frac{\omega_m}{\omega_m^*} = \frac{4\pi^2 f_c f_\omega \frac{\hat{J}}{J}}{\left(s+2\pi f_\omega\frac{\hat{J}}{J}\right)(s+2\pi f_c)} \tag{23}$$

$$\frac{\omega_m}{T_L} = -\frac{\frac{1}{J}s}{\left(s+2\pi f_\omega\frac{\hat{J}}{J}\right)\left(s+\frac{\widehat{K_f}}{J}\right)} \tag{24}$$

by setting $k_{p\omega} = 2\pi f_\omega \hat{J}$, $T_\omega = \frac{\hat{J}}{\widehat{K_f}}$.

Comparing (21) with (23), it can be found that the closed loop tracking transfer functions of the modified method with active damping and the conventional method without active damping are the same. However, the dominant closed-loop pole of the anti-disturbance transfer function is moved from $s = -\frac{\widehat{K_f}}{J}$ in (24) to $s = -\frac{K_{fa}}{J}$ in (22) after the active damping is applied. Therefore, with properly tuned PI parameters $k_{p\omega} = \frac{2\pi f_\omega \hat{J}}{\frac{3P\psi_m}{2}}$, $T_\omega = \frac{\hat{J}}{K_{fa}}, k_{pi} = 2\pi f_c \widehat{L_q}, T_i = \frac{\widehat{L_q}}{\widehat{R_s}}$, the active damping scheme enhances the stability and anti-disturbance capability of the speed controller while keeping the reference tracking capability unchanged. The corresponding bodes diagrams of (21) and (22) are presented in Fig.3 and Fig.4, respectively.

In Fig.3, the bode diagram of the tracking transfer function ω_m/ω_m^* are compared at different speed bandwidths $f_\omega = 25Hz, 50Hz, 100Hz$ and current loop bandwidths $f_c = 250Hz, 1000Hz$. In Fig.4, the bode diagram of the anti-disturbance transfer function ω_m/T_L are compared at different speed loop bandwidths $f_\omega = 25Hz, 50Hz, 100Hz$ and damping ratios $K_{fa} = 0.1, 1.0, 10.0$. Fig.3 reveals that the speed loop cutoff frequency is dominated by the speed loop bandwidth f_ω. Fig.4 shows that active damping contributes to obviously improved suppression effects of low-frequency disturbance for the speed controller, and a larger active damping ratio means better anti-disturbance capability. With $K_{fa2} = 10$, the amplitude gains of ω_m/T_L are all decreased by 25dB compared to $K_f = 0.1$ at the three different f_ω.

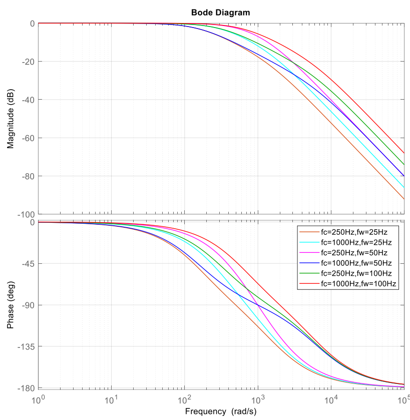

Fig.3 Bode diagram of ω_m/ω_m^*

In particular, the low-frequency amplitude gains of $f_\omega = 25Hz, K_{fa2} = 10$ is even smaller than that of $f_\omega = 100Hz, K_f = 0.1$. However, a larger active damping ratio also results in a larger integral gain according to $k_{p\omega} = 2\pi f_\omega \hat{J}/(3P\psi_m/2)$, $T_\omega = /K_{fa}$, which increases the chance of speed loop saturation considering the output limit. Therefore, a compromise must be made regarding the active damping and PI parameter tuning. Also, $H_{ad}(s)$ contains a parameter f_c regarding the bandwidth of the current loop, so the current loop and speed loop control parameters need to be tuned together.

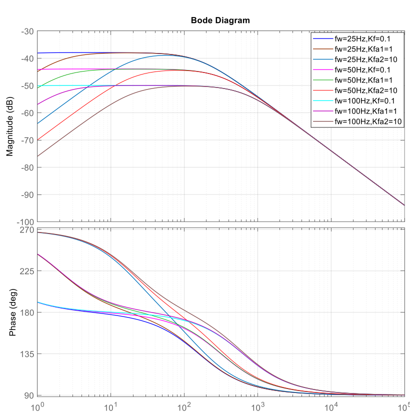

Fig.4 Bode diagram of ω_m/T_L

B. Adaptive Saturation Voltage Limit of Current loops

The previous analysis assumes the current loops are not saturated and the d,q-axis current can well follow the references. However, for machines with low inductance, the large current and limited dc-link voltage easily get the controller saturated since the current cannot track the reference in the transient due to the cross-coupling between d,q axis when the error between current reference and feedback is large, which normally happens at sudden load change. At saturation conditions, the voltage output is clamped to the saturation limit value determined by the dc supply voltage and the modulation algorithms. In the conventional PI approach, the d,q-axis voltage reference amplitude $\sqrt{v_d^2 + v_q^2}$ are saturated at $v_{dc}/\sqrt{3}$ (SVPWM) or $v_{dc}/2$(SPWM), which easily leads to instant over-current at a lower speed with smaller back-EMF due to small inductance and resistance, and thus cause instant torque spike and speed overshoot.

In this paper, the saturation voltage reference limit of current loops adaptive to the instant speed as shown in

$$v_{max} = \min\left(\omega_r\psi_{\mathrm{m}} + R_s i_{max}, m_{max} v_{dc}\right) \quad (25)$$

is proposed to limit the maximum current to prevent overcurrent in transient process and eliminate the torque spike and ensure a stable performance at wide speed range operation. The saturation limit v_{max} of current loops in (25) is the minimum value of $\omega_r\psi_{\mathrm{m}} + R_s i_{max}$ adaptive to the back EMF and maximum allowed current i_{max}, and the maximum inverter output voltage $m_{max}v_{dc}$ determined by the dc-link voltage v_{dc} and the maximum modulation rate m_{max} dependent on modulation algorithms. The saturation limit curves at $i_{max} = 150A$, $250A$, $500A$ are shown in Fig.5 with $v_{dc} = 270V$, $m_{max} = \frac{1}{\sqrt{3}}$ (SVPWM),1/2(SPWM), $R_s = 0.1\Omega$, $\psi_{\mathrm{m}} = 0.0364Vs$ .The intersection between $m_{max}v_{dc}$ and $\omega_r\psi_{\mathrm{m}} + R_s i_{max}$ determines the saturation limit region at the certain allowed maximum current.

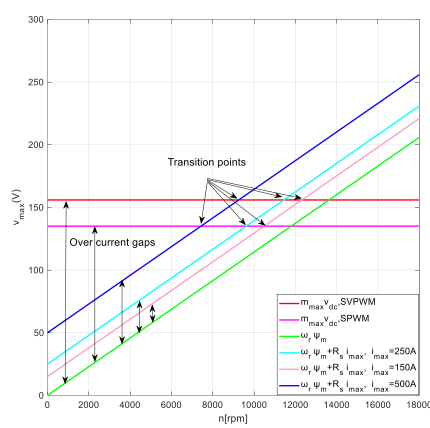

Fig.5 Adaptive voltage saturation limit

To evaluate the performance of the proposed adaptive voltage limit scheme, the current and voltage limit circle equations are derived as

$$\begin{cases} i_d^2 + i_q^2 < i_N^2 \\ (\psi_m + L_d i_d + \frac{R_s}{\omega_r} i_q)^2 + (\frac{R_s}{\omega_r} i_d - L_q i_q)^2 < r^2 \end{cases} \quad (26)$$

where i_N is the nominal current of the machine, and r is the radius of the voltage limit circle $r = \frac{v_{max}}{\omega_r}$. Normally R_s is neglected when analyzing the voltage limit circle, but it cannot be neglected here for the case of a machine with low inductance.

Denoting $\frac{R_s}{\omega_r} = \alpha$, then the voltage limit circle equation can be expressed in polar coordinates as

$$\begin{cases} \alpha i_d - L_q i_q = r cos\theta \\ L_d i_d + \alpha i_q = r sin\theta - \psi_m \end{cases} \quad (27)$$

Solving (27), the boundary of d,q-axis current limited by the voltage circle is obtained as

$$\begin{cases} i_q = \frac{\alpha(r sin\theta - \psi_m) - L_d r cos\theta}{L_d L_q + \alpha^2} \\ i_d = \frac{L_q(r sin\theta - \psi_m) + \alpha r cos\theta}{L_d L_q + \alpha^2} \end{cases} \quad (28)$$

As α and r are speed-dependent, the voltage limit circles at different speeds from 2 krpm to 18 krpm are compared. Three cases $v_{max1} = m_{max} v_{dc}$, $v_{max2} = \psi_m \omega_r + R_s i_{max}$, $v_{max3} =$ min (v_{max1}, v_{max2}) are considered, and the results are presented in Fig.6 to Fig.8, respectively. SVPWM is considered here, so $m_{max} = 1/\sqrt{3}$. i_{max} is set as 250A although i_N is around 150A to leave some margin for instant overload. Each circle determines the d,q-axis current boundary at a certain speed when the output voltage of the current loop is saturated to the corresponding voltage.

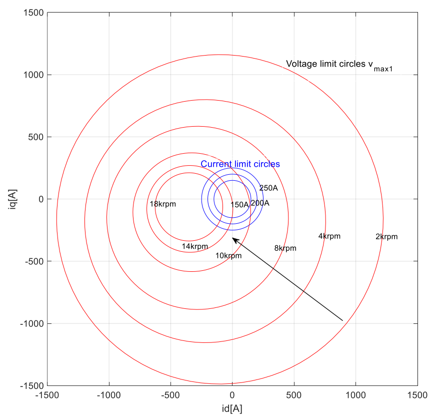

Fig.6 voltage limit circle $v_{max1} = m_{max} v_{dc}$ at different speeds

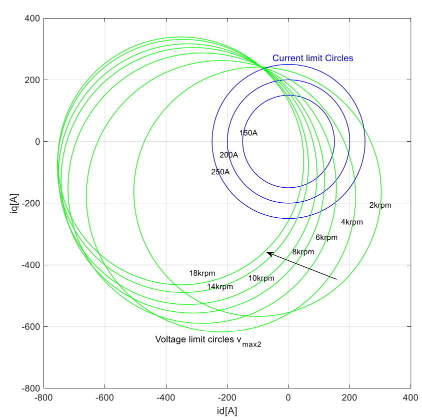

Fig.7 voltage limit circle with $v_{max2} = \psi_m \omega_r + R_s i_{max}$ at different speeds

In Fig.6, the maximum d,q axis currents can be up to over 1000A at 2krpm, even if a current limit of 250A is applied to the current loop. The maximum d,q-axis currents at 4 krpm and 8krpm are also far beyond 250 A, which reveals a high risk of over current. In Fig.7, the d,q-axis current are much reduced at 2 krpm to 8 krpm with the speed adaptive voltage limit applied, but the circle limited by v_{max1} is smaller at higher speeds. The transition point around 12 krpm can be seen in Fig 8, which proves that the current is limited at saturation conditions within wide speed range, and thus intolerable over-current and torque spikes are prevented.

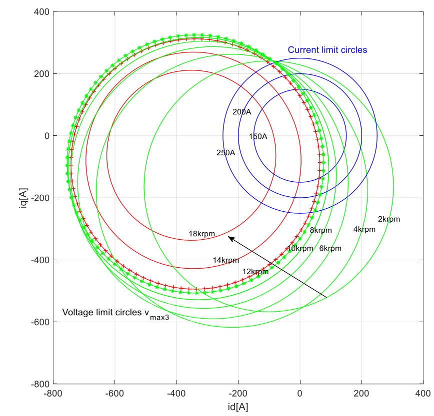

Fig.8 voltage limit circle with $v_{max3} = \min(v_{max1}, v_{max2})$ at different speeds

Combining the active damping and adaptive voltage saturation limit, the diagram of the proposed method is presented in Fig.9, whereas the speed and current controllers are expressed in (29) to (37) as follows

$$i_d^* = k_{pf}\left(1 + \frac{1}{T_f s}\right)\left(m_{max} v_{dc} - v_{dq}^*\right) + \frac{k_{b\omega}}{s}\left(i_{d,sat}^* - i_d^*\right) \quad (29)$$

$$i_q^* = k_{p\omega}\left(1 + \frac{1}{T_\omega s}\right)\left(\omega_m^* - \omega_m\right) - H_{ad}(s) + \omega_m \frac{k_{b\omega}}{s}\left(i_{q,sat}^* - i_q^*\right) \quad (30)$$

$$i_{d,sat}^* = \begin{cases} i_d^*, i_d^* \le 0 \\ 0, i_d^* > 0 \end{cases} \quad (31)$$

$$i_{q,sat}^* = \begin{cases} i_{sat}, i_q^* > i_{sat} \\ i_q^*, -i_{sat} \le i_q^* \le i_{sat} \\ -i_{sat}, i_q^* < -i_{sat} \end{cases} \quad (32)$$

$$v_d^* = k_{pi}\left(1 + \frac{1}{T_i s}\right)\left(i_{d,sat}^* - i_d\right) - \omega_r L_q i_q + \frac{k_{bc}}{s}\left(v_{d,sat}^* - v_d^*\right) \quad (33)$$

$$v_q^* = k_{pi}\left(1 + \frac{1}{T_i s}\right)\left(i_{q,sat}^* - i_q\right) + \omega_r\left(\psi_m + L_d i_d\right) + \frac{k_{bc}}{s}\left(v_{q,sat}^* - v_q^*\right) \quad (34)$$

$$v_{dq}^* = \sqrt{\left(v_d^{*2} + v_q^{*2}\right)} \quad (35)$$

$$v_{d,sat}^* = \begin{cases} v_d^*, v_{dq}^* \le v_{max} \\ v_d^* * \frac{v_{max}}{v_{dq}^*}, v_{dq}^* > v_{max} \end{cases} \quad (36)$$

$$v_{q,sat}^* = \begin{cases} v_q^*, v_{dq}^* \le v_{max} \\ v_q^* * \frac{v_{max}}{v_{dq}^*}, v_{dq}^* > v_{max} \end{cases} \quad (37)$$

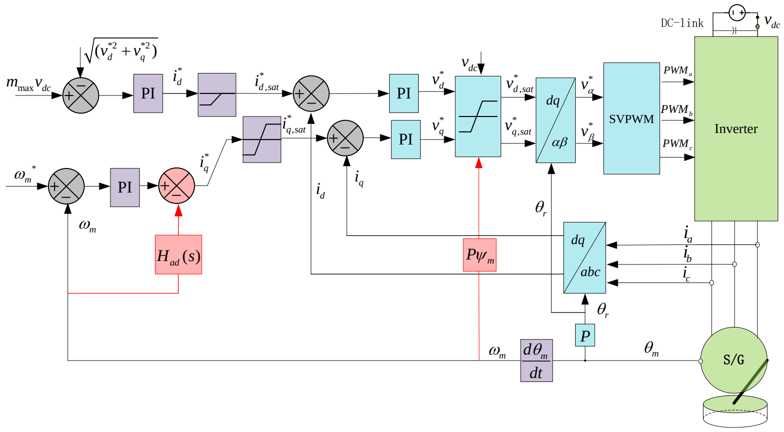

Fig.9 Diagram of the proposed method with active damping and adaptive voltage saturation limit

Field weakening is applied for the d-axis current reference in (29), whereas the back-calculation anti-windup method is applied in both the speed loop controller (30) and current loop controller (33) and (34). An improved anti-windup scheme as proposed in [38] is adopted to improve the dc bus voltage usage by saturating the root mean square value of the voltage reference to v_{max} by (35)-(37).

IV. Simulation Results

For tradeoff studies, the proposed modified method with active damping and adaptive saturation limit is compared with the conventional PI method through simulation at different switching frequencies. Parameters of the machine used in the simulation are listed in TABLE II in Section II. Fig.10 to Fig. 13 present simulation results of speed step response from 0 rpm to 6krpm and 6krpm to 10krpm at a switching frequency of 16 kHz (SiC IGBT) and 40 kHz (SiC MOSFET), respectively, of both the conventional PI method and the proposed modified method. It can be seen in Fig.10 that the dynamic response of the proposed method is much faster than that of the conventional method at both 16 kHz and 40 kHz when the speed reference steps from 0 rpm to 6 krpm and from 6 krpm to 10 krpm.

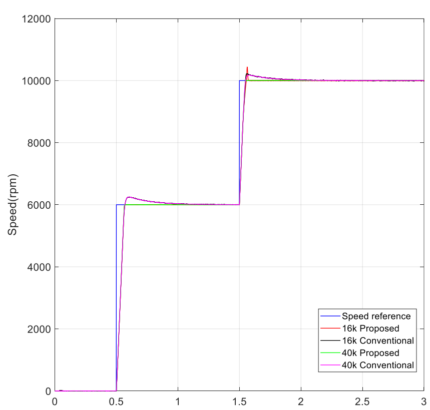

Fig.10 Simulation results of speed step responses

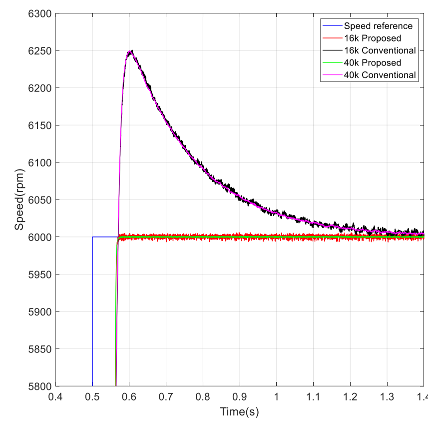

Fig.11 Simulation results of a speed step response from 0 rpm to 6000 rpm (zoomed)

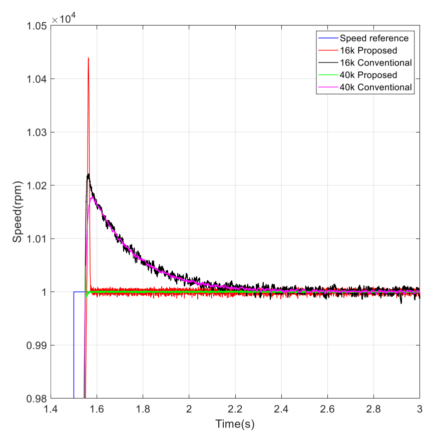

Fig.12 Simulation results of a speed step response from 6000 rpm to 10000rpm (zoomed)

The zoomed view in Fig.11 shows the response time of the proposed method is only 0.06 s when the speed reference steps from 0 rpm to 6 krpm, whereas the response time of the conventional method is almost 0.9 s. Similarly, the zoomed view in Fig.12 shows the response time of the proposed method is less than 0.05 s when the speed reference steps from 6 rpm to 10 krpm, whereas the response time of the conventional method is almost 0.9 s. In particular, the dynamic response of the proposed method at 16 kHz switching frequency is much better than that of the conventional method at 40 kHz. The accelerated dynamic response is due to the increased integral gain for pole-zero cancellation when the active damping is applied.

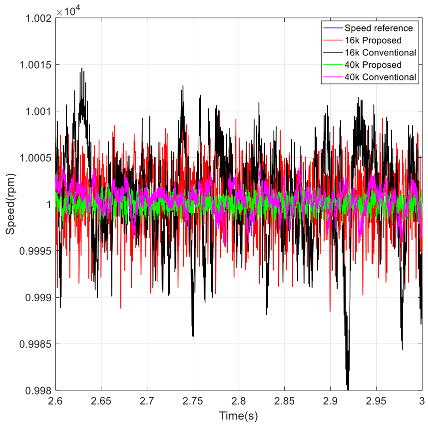

Fig.13 Simulation results of speed steady state ripples at 10000rpm (zoomed)

As for the steady-state speed ripples, it can be found in Fig.13 that the speed ripples are effectively reduced at both 16kHz and 40kHz with the proposed modifications applied. The performance of 16 kHz can be further improved by increasing the active damping gain. The simulation results prove the effectiveness of the proposed modification in reducing the speed ripples and accelerating the dynamic response of the speed loop. Although the performance at 16 kHz is not as good as that at 40 kHz, the purpose of this paper is not to challenge the widegap devices of higher switching frequency with the proposed method, but to provide an alternative to reduce the torque ripple and speed ripple to improve the performance of the system through a modified control method based on limitations of the hardware.

V. Experimental Results

A. Test Setup description

The proposed method with active damping and adaptive saturation limit is verified on a PMS/G prototype with an inductance of 99uH and a switching frequency of 16 kHz. Parameters of the PMS/G and inverter are listed in Table II in Section II, whereas the hardware structure is presented in Fig. 14.

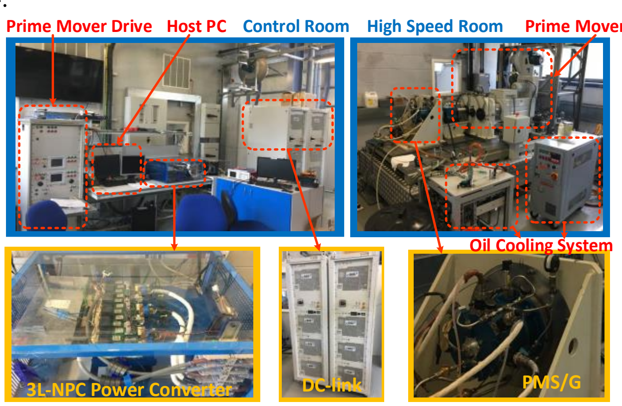

Fig.14 PMS/G test rig setup

A 150 kW prime mover and the homebrewed PMS/G machine are placed in an isolated room from the safety viewpoint. The three-level Neutral Point Clamped (NPC) converter along with a DSK6713/Actel a3p400 control platform, dc source, prime mover controller, and host PC is placed in the control room. The selected devices for the NPC converter are IGBT modules from Infineon. The prime mover emulates an aircraft engine shaft, coupled with the PMS/G. The NPC converter interfaces the PMS/G and the 270 V dc link. Real-time variables of the inverter are monitored by the host PC through a data cable.

B. Experimental Results

The proposed method with active damping and adaptive saturation limit is compared with the conventional method at different speeds 14 krpm, 10 krpm, 6 krpm and 2 krpm, respectively, with a light load of 1N*m, which is the condition the torque ripples and speed ripples cause the most serious mechanical vibration and noises.

The speed and torque waveforms at 14 krpm are presented in Fig.15 and Fig.16, respectively, where the waveforms of the proposed method are in red, whereas that of the conventional method are in blue. The steady-state speed ripple peak-to-peak value of the conventional method is roughly 50 rpm, whereas that of the proposed method is less than 20 rpm. The torque ripple peak-to-peak value is reduced from 9 N*m to less than 3 N*m. The torque FFT results at 14 krpm in Fig.17 shows that the low-frequency harmonics under 400 Hz are effectively suppressed with the proposed modifications applied, which matches the theoretical analysis in Section III.

The speed and torque waveforms at 10krpm are presented in Fig.18 and Fig.19, respectively. With the proposed method, the steady-state speed ripples are reduced from 70rpm to 20 rpm, whereas the torque ripples are reduced from 13 N*m to less than 4 N*m. The Torque FFT results at 10 krpm in Fig.20 are similar to Fig.17 of 14 krpm where the low-frequency harmonics under 200 Hz are effectively suppressed with the proposed modifications applied. The spike at 200 Hz is shifted to 400Hz with reduced magnitude. The reason why performance at 14krpm is slightly better than 10k rpm is that the PMS/G enters the field weakening region at 14krpm with non-zero d-axis current reference, and the q-axis current saturation limit is reduced.

The speed and torque waveforms at 6 krpm are presented in Fig.21 and Fig.22, respectively. The steady-state speed ripples are reduced from 70 rpm to 30 rpm, whereas the torque ripples are reduced from 8 N*m to less than 4 N*m. Torque FFT results in Fig.23 shows the low-frequency ripples are generally suppressed with the proposed algorithm applied, although there is a spike at 100 Hz. As for the results at 2 krpm, the steady-state speed ripples are reduced from 70rpm to 30 rpm in Fig.24. The torque ripple results in Fig.25 show an obvious reduction of peak-to-peak value, as the modulation index is rather low at this speed, resulting in a lot of harmonics in the current. But the torque ripples are shifted to higher frequency according to FFT results in Fig.26 so that the peak of torque integral value is reduced, which results in a reduction of speed ripples in Fig.24.

In conclusion, the speed ripple and torque ripple peak-to-peak values at different speeds are summarized in TABLE III and TABLE IV, respectively. In general, the steady-state speed ripples of the PMS/G are reduced by at least 57.1% with the

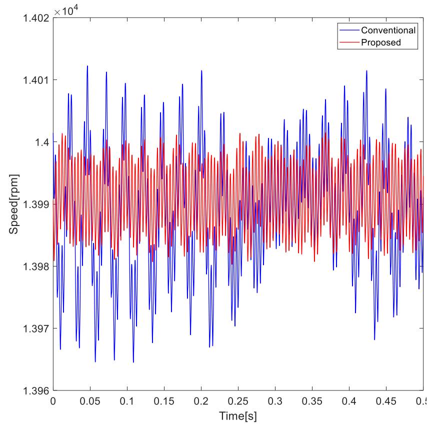

Fig.15 Speed waveforms at 14 krpm

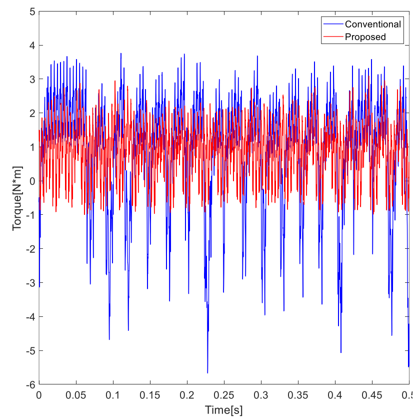

Fig.16 Torque waveforms at 14 krpm

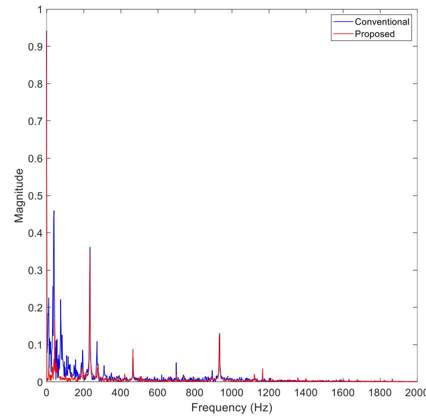

Fig.17 Torque FFT at 14 krpm

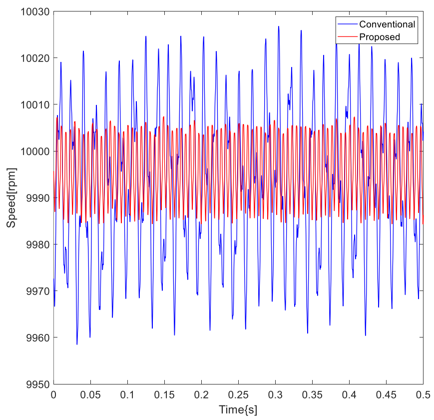

Fig.18 Speed waveforms at 10 krpm

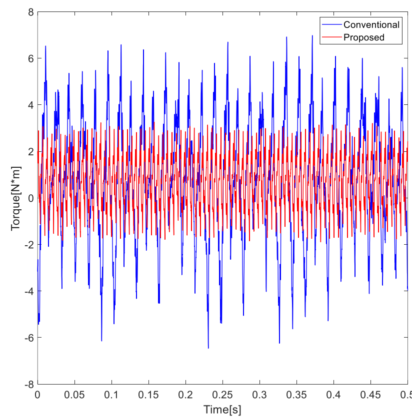

Fig.19 Torque waveforms at 10 krpm

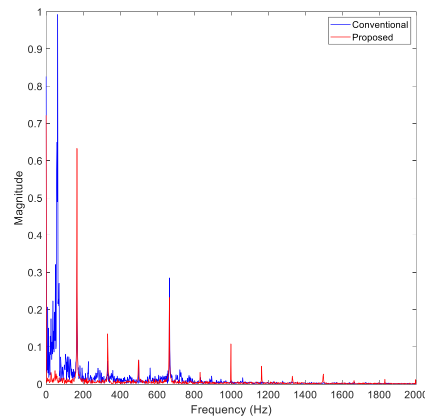

Fig.20 Torque FFT at 10 krpm

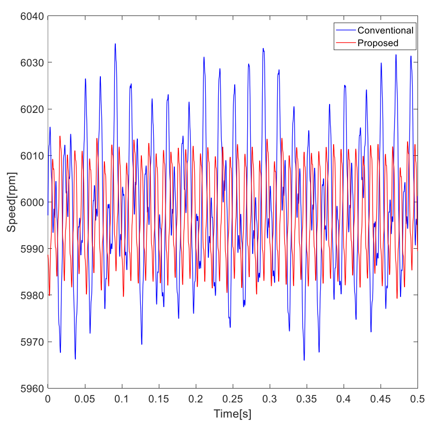

Fig.21 Speed waveforms at 6 krpm

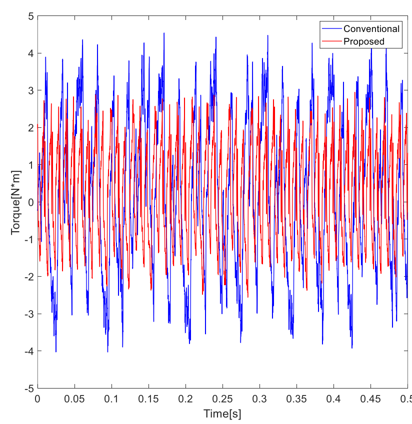

Fig.22 Torque waveforms at 6 krpm

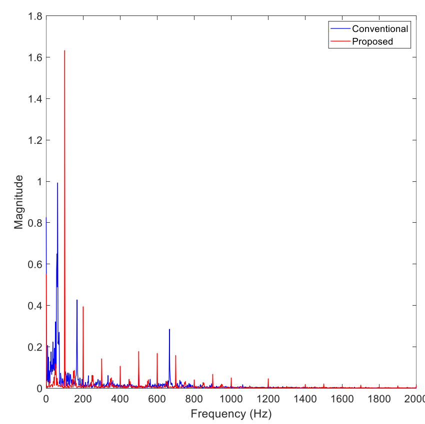

Fig.23 Torque FFT at 6 krpm

TABLE III
SPEED RIPPLE PEAK-TO-PEAK

	Conventional methods(rpm)	Proposed methods(rpm)	Reduction Rate
14 krpm	50	20	60.0%
10 krpm	70	20	71.4%
6 krpm	70	30	57.1%
2 krpm	70	30	57.1%

TABLE IV
TORQUE RIPPLE PEAK-TO-PEAK

	Conventional methods(N*m)	Proposed methods(N*m)	Reduction Rate
14 krpm	9	3	66.7%
10 krpm	13	4	69.2%
6 krpm	8	4	50.0%
2 krpm	6	6	0.0%

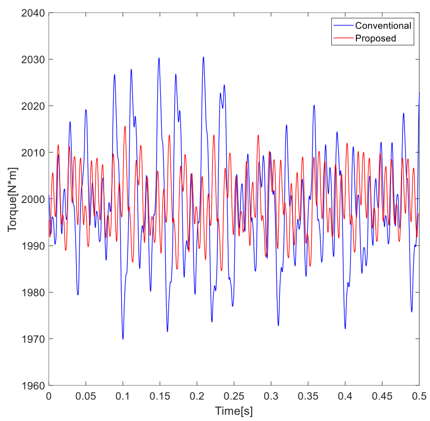

Fig.24 Speed waveforms at 2 krpm

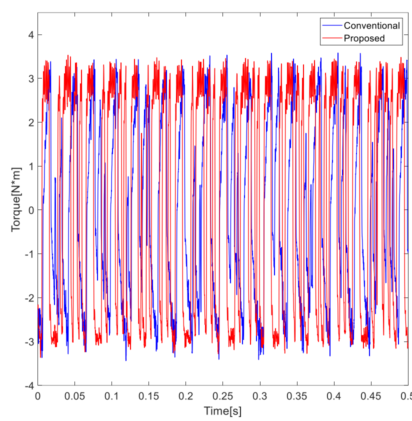

Fig.25 Torque waveforms at 2 krpm

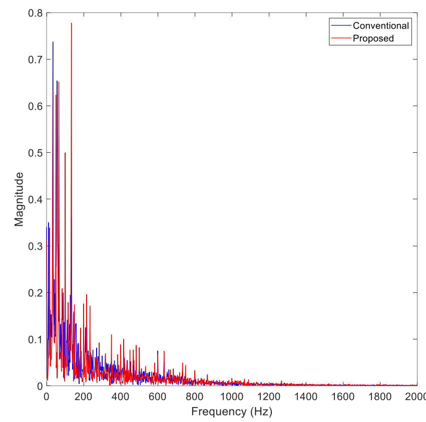

Fig.26 Torque FFT at 2 krpm

active damping and adaptive saturation limit applied within a wide speed range from 2 krpm to 14 krpm. As for the torque ripples, the peak-to-peak value is reduced by at least 50.0 % from 6krpm to 14 krpm. The performance at high speed is better than low speed as the low modulation ratio at low-speed results in current distortion and harmonics which cannot be solved through pure control methods. An optimized modulation algorithm can be applied to further improve the low-speed performance.

V. CONCLUSION

In 270V onboard power systems, the high-speed PMS/Gs are designed to be with low inductance and resistance, which results in severe torque ripples, and may further lead to speed oscillation and generate severe vibrations and noises that are harmful to the mechanical system and human beings around. The low inductance and resistance also increase the risk of overcurrent in case of current controller saturation, especially at a lower speed with relatively lower back-EMF. A modified speed/torque ripple reduction method for high-speed PMS/Gs with low inductance within the PI-based FOC frame is proposed in this paper to improve their performance within the wide speed range. As the torque ripple is a disturbance of the speed loop, an active damping scheme is applied to the speed loop to increase the anti-disturbance capability and generate a smoother reference for the current loop. Different forms of active damping are compared, based on which parameter tuning criteria are concluded. Overcurrent issues at current controller saturation are considered, an adaptive output voltage saturation limit is proposed, and a back-calculation anti-windup strategy is utilized for the current loop to limit the peak value of current to prevent instant overcurrent and torque spikes. Both the active damping and adaptive saturation limit contribute to reducing the speed and torque ripples. Tradeoff study through simulation between an IGBT based inverter with a switching frequency of 16 kHz and a MOSFET based inverter with a switching frequency of 40 kHz show that the proposed modified method not only reduces the speed ripples at steady states but also improves the dynamic response of the speed loop. Finally, the proposed method is validated on a high-speed PMS/G test rig with an inductance of 99 uH and a switching frequency of 16 kHz. The results show that the speed and torque ripples are effectively reduced over 50% within the speed range from 2 krpm to 14 krpm.

REFERENCES

[1] M. LUKIC, P. GIANGRANDE, A. HEBALA, S. NUZZO, AND M. Galea, "Review, challenges, and future developments of electric taxiing systems," IEEE Trans. Transp. Electrific., vol. 5, no. 4, pp. 1441–1457, Dec. 2019.

[2] E. Sayed, M. Abdalmagid, G. Pietrini, N.M. Sa'adeh, A. D. Callegaro, C. Goldstein, A. Emadi, "Review of Electric Machines in More-/Hybrid-/Turbo-Electric Aircraft," IEEE Trans. Transp. Electrific., vol. 7, no. 4, pp. 2976–3005, Dec. 2021.

[3] B. K. Bose, "Global energy scenario and impact of power electronics in 21st century," IEEE Trans. Ind. Electron., vol. 60, no. 7, pp. 2638–2651, Jul. 2013.

[4] A. Battiston, E.-H. Miliani, S. Pierfederici, and F. Meibody-Tabar, "Efficiency improvement of a quasi-Z-source inverter-fed permanent-magnet synchronous machine-based electric vehicle," IEEE Trans. Transport. Electrific., vol. 2, no. 1, pp. 14–23, Mar. 2016.

[5] B. Sarlioglu and C. T. Morris, "More electric aircraft: Review, challenges, and opportunities for commercial transport aircraft," IEEE Trans. Transp. Electrific., vol. 1, no. 1, pp. 54–64, Jun. 2015.

[6] P. Giangrande et al., "Considerations on the development of an electric drive for a secondary flight control electromechanical actuator," IEEE Trans. Ind. Appl., vol. 55, no. 4, pp. 3544–3554, Jul./Aug. 2019.

[7] Y. Wang, S. Nuzzo, H.Zhang, W. Zhao, C. Gerada, M. Galea. "Challenges and Opportunities for Wound Field Synchronous Generators in Future More Electric Aircraft," IEEE Trans. Transp. Electrific., vol. 6, no. 4, pp. 1466–1477, Dec. 2020.

[8] F. Guo, T. Yang, A. M. Diab, S. S. Yeoh, S. Bozhko, P. Wheeler, "An Enhanced Virtual Space Vector Modulation Scheme of Three-Level NPC Converters for More-Electric-Aircraft Applications," IEEE Trans. Ind. Appl., vol. 57, no. 5, pp. 5239–5251, Sep./Oct. 2021.

[9] S. S. Yeoh, T. Yang, L. Tarisciotti, C. I. Hill, S. Bozhko, and P.Zanchetta, "Permanent-Magnet Machine-Based Starter–Generator System With Modulated Model Predictive Control ," IEEE Trans. Transp. Electrific., vo3, no. 4, pp. 878–890, Dec. 2017.

[10] P. Wheeler and S. Bozhko, "The more electric aircraft: Technology and challenges," IEEE Electrific. Mag., vol. 2, no. 4, pp. 6–12, Dec. 2014.

[11] S.-C. Carpiuc and C. Lazar, "Fast real-time constrained predictive current control in permanent magnet synchronous machine-based automotive traction drives," IEEE Trans. Transport. Electrific., vol. 1, no. 4, pp. 326–335, Dec. 2015.

[12] K. D. Hoang and H. K. A. Aorith, "Online control of IPMSM drives for traction applications considering machine parameter and inverter nonlinearities," IEEE Trans. Transport. Electrific., vol. 1, no. 4, pp. 312–325, Dec. 2015.

[13] F. Gao, X. Zheng, S. Bozhko, C. I. Hill, and G. Asher, "Modal analysis of a PMSG-based DC electrical power system in the more electric aircraft using eigenvalues sensitivity," IEEE Trans. Transport. Electrific., vol. 1, no. 1, pp. 65–76, Jun. 2015.

[14] F. Guo, T. Yang, A. M. Diab, S. S. Yeoh, C. Li, S. Bozhko, P. Wheeler, “An Over modulation Algorithm With Neutral-Point Voltage Balancing for Three-Level Converters in High-Speed Aerospace Drives,” IEEE Trans. Power Electron.,vol.37,no.2,pp. 2021-2032, Feb.2022
[15] V. Madonna , P. Giangrande, M. Galea., “Electrical Power Generation in Aircraft: review, challenges and opportunities,” IEEE Trans. Transport. Electrific., vol. 4, no. 3, pp. 646–659, May. 2018.
[16] D. A. Gonzalez, D. M. Saban, “Study of the Copper Losses in a High-Speed Permanent-Magnet Machine With Form-Wound Windings,” IEEE Trans. Ind. Electron, vol. 61, no. 6, pp.3038-3045, June 2014
[17] M. Leandro, N. Bianchi, M. Molinas, and R. B. Ummaneni, “Low inductance effects on electric drives using slotless permanent magnet motors: A framework for performance analysis,” in Proc. IEEE Int. Electr. Mach. Drives Conf. (IEMDC), pp. 1099–1105,2019.
[18] X. Li, X. Wang, P. Gao, Y. Gu, “Model Predictive Current Control Algorithm Based on Joint Modulation Strategy for Low-Inductance PMSM”, IEEE Trans. Power Electron., vol. 37, no. 1, pp. 806–819, Jan. 2022.
[19] Y. Hu, S.Zhu, L. Xu, B. Jiang, “Reduction of Torque Ripple and Rotor Eddy Current Losses by Closed Slots Design in a High-speed PMSM for EHA Applications,” IEEE Trans. Magn., vol. 58, no. 2, Feb. 2022
[20] G. Liu, X. Du, W. Zhao, Q. Chen, “Reduction of Torque Ripple in Inset Permanent Magnet Synchronous Motor by Magnets Shifting,” IEEE Trans.Magn., vol.53, no.2, Fed.2017
[21] J. Holtz and L. Springob, “Identification and compensation of torque ripple in high-precision permanent magnet motor drives,” IEEE Trans. Ind. Electron., vol. 43, no. 2, pp. 309–320, Apr. 1996.
[22] G. Heins, M. Thiele, and T. Brown, “Accurate torque ripple measurement for PMSM,” IEEE Trans. Instrum. Meas., vol. 60, no. 12, pp. 3868–3874, Dec. 2011.
[23] N. Matsui, T. Makino, and H. Satoh, “Autocompensation of torque ripple of direct drive motor by torque observer,” IEEE Trans. Ind. Appl., vol. 29, no. 1, pp. 187–194, Jan. 1993.
[24] M. Tang, A. Formentini, S. A. Odhano, P. Zanchetta, “Torque Ripple Reduction of PMSMs Using a Novel Angle-Based Repetitive Observer,” IEEE Trans. Ind. Electron., vol.67, no.4, pp. 2689 – 2699, Apr. 2020
[25] S. Hara, Y. Yamamoto, T. Omata, and M. Nakano, “Repetitive control system: A new type servo system for periodic exogenous signals,” IEEE Trans. Autom. Control, vol. 33, no. 7, pp. 659–668, Jul. 1988.
[26] W. Qian, S. K. Panda, and J.-X. Xu, “Torque ripple minimization in PM synchronous motors using iterative learning control,” IEEE Trans. Power Electron., vol. 19, no. 2, pp. 272–279, Mar. 2004.
[27] Y.Wang, F. Gao, and F. J. Doyle III, “Survey on iterative learning control, repetitive control, and run-to-run control,” J. Process Control, vol. 19, no. 10, pp. 1589–1600, 2009.
[28] P. Mattavelli, L. Tubiana, and M. Zigliotto, “Torque-ripple reduction in PM synchronous motor drives using repetitive current control,” IEEE Trans. Power Electron., vol. 20, no. 6, pp. 1423–1431, Nov. 2005.
[29] S. Bolognani, L. Tubiana, and M. Zigliotto, “Sensorless control of PM synchronous motors with nonsinusoidal back EMF for home appliance,” in Proc. IEEE Int. Electr. Mach. Drives Conf., 2003, pp. 1882–1888.
[30] Y. Ren and Z. Q. Zhu, “Reduction of Both Harmonic Current and Torque Ripple for Dual Three-Phase Permanent-Magnet Synchronous Machine Using Modified Switching-Table-Based Direct Torque Control,” IEEE Trans. Ind. Electron., vol.62, no.11, pp.6671-6683, June 2015
[31] Y. Cho, Y. Bak and K.B. Lee, “Torque-Ripple Reduction and Fast Torque Response Strategy for Predictive Torque Control of Induction Motors,” IEEE Trans. Power Electron., vol.33, no.3, pp.2458-2470, Apr. 2017
[32] L. A. Adase, I. M. Alsofyani and K.B. Lee, “Predictive Torque Control with Simple Duty-Ratio Regulator of PMSM for Minimizing Torque and Flux Ripples,” IEEE Access, vol.8, pp.2373-2381, Dec. 2020
[33] Z. Zhou, C. Xia, Y. Yan, Z. Wang and T. Shi, “Torque Ripple Minimization of Predictive Torque Control for PMSM With Extended Control Set,” IEEE Trans. Ind. Electron., vol.64, no.9, Sept. 2017
[34] M. Siami, D.A. Khaburi and J. Rodríguez, “Torque Ripple Reduction of Predictive Torque Control for PMSM Drives with Parameter Mismatch,” IEEE Trans. Power Electron., vol.32, no.9, Sept.2017
[35] S. Bozhko, T. Yang et al., "Development of Aircraft Electric Starter–Generator System Based on Active Rectification Technology," IEEE Trans. Transport. Electrific., vol. 4, no. 4, pp. 985-996, Dec. 2018,
[36] P. A. Dahono, “A control method to damp oscillation in the input LC filter of AC-DC PWM converters”, 33rd Annual IEEE Power Electron. Specialists Conf., vol. 4, 2002, pp. 1630-1635.
[37] P. A. Dahono, “A control method for DC-DC converter that has an LCL output filter based on new virtual capacitor and resistor concepts”, 35th Annual IEEE Power Electron. Specialists Conf., Aachen, Germany, vol. 1, 2004, pp. 36-42
[38] Y.-s. Jeong and S.-K. Sul, "Analysis and design of a decoupling current controller for AC machines: a unified transfer-matrix approach," in Fourtieth IAS Annual Meeting. Conf. Record of the 2005 Ind. Appl. Conf., 2005, vol. 1, pp. 751-758: IEEE

Xiang Zhang received the B.S. degree in electrical engineering and automation from Zhejiang University (ZJU), Hangzhou, China in July 2013, and a double Ph.D. degree in electrical engineering from ZJU and the Université Libre de Bruxelles (ULB), Brussels, Belgium, in March 2019. He worked as a Research Fellow with the Power Electronics, Machines and Controls Research Group, University of Nottingham, Nottingham, U.K., from May 2019 to May 2022. Since June 2022, he has been a Senior Motor Controls Engineer at Turntide Technologies, Gateshead, U.K. His research interests include the drive and control of high-speed electrical machines for flywheel, electrical vehicle and more electrical aircraft applications.

Tao Yang (SM’20) received his MEng Degree from Shanghai Jiao Tong University, China in 2008 and his Ph.D. degree in electrical engineering from the University of Nottingham, U.K. in 2013.

Since 2013, he has been a Researcher with Power Electronics, Machines and Control Group, University of Nottingham, where he became an Assistant Professor in 2016, and an Associate Professor in 2019. His research interests include high-speed electric motor drive control, power electronic conversion, electrical system design and optimization for more electric/hybrid/all-electric aircraft applications. His PhD research within EU Clean Sky on “Modelling electrical power system for more-electric aircraft applications” has resulted in him winning the inaugural “Clean Sky Best PhD Award” in 2016. Dr. Yang is an Associate Editor for the IEEE Transactions on Transportation Electrification and Chinese Journal of Aeronautics.

Serhiy Bozhko (Senior Member, IEEE) received the M.Sc. and Ph.D. degrees in electromechanical systems from the National Technical University of Ukraine, Kyiv City, Ukraine, in 1987 and 1994, respectively. Since 2000, he has been with the Power Electronics, Machines and Controls Research Group, University of Nottingham, U.K., where he is currently a professor of aircraft electric power systems and the Director of the Institute for Aerospace Technology. He is leading several EU- and industry funded projects in the area of aircraft electric power systems, including power generation, distribution and conversion, power quality, control and stability issues, power management and optimization, as well as advanced modelling and simulations methods.